

Real-Time 4D Deformable Image Registration Using Feature-Based Adaptive Tetrahedral Mesh

Abstract. In this paper we propose a finite element method (FEM)-based deformable image registration (DIR) method for 4D (i.e., 3D images in different phases) images, with fast computational speed and high accuracy. Firstly, the adaptive tetrahedral mesh is generated based on the image features of the reference phase image. Subsequently, the deformation vector fields (DVF) and deformed images of 4D images can be obtained through an optimization of matching each phase of the target 4D images with the corresponding deformed reference phase image in an intensity-based scheme with mesh-based regularity. The proposed 4D DIR method is designed and implemented on GPU, resulting in significantly increasing the computational efficiency due to its parallel computing ability. Finally, both the DVFs and deformed images are well computed in almost real time, and can be used in high-quality 4D images and motions visualization, tumor tracking, and organ segmentation. The performance of the proposed algorithm is evaluated on a 4D NCAT phantom and a clinical pulmonary 4D CT images. Our results are compared qualitatively and quantitatively with the state-of-the-art in DIR on several examples by using the standard measurement criteria.

Keywords: Deformable image registration, adaptive tetrahedral mesh, 4D images, GPU

1 Introduction

Nowadays, deformable image registration (DIR) has been employed as an automated and effective segmentation method to transfer tumor or organ contours from the planning image to daily images, instead of manual segmentation. A major technical bottleneck for the clinical implementation of online adaptive radiation therapy (ART) is the requirement of real-time image segmentation. Besides that, high-fidelity modeling the 3D shapes of the tumor and surrounding organs and tissues in real-time for tracking their deformations and motions accurately at different respiration phases become important in radiation therapy. To realize the clinical application of DIR, much effort has been invested to develop fast and accurate algorithms, such as demons, i.e., one commonly used DIR algorithm, introduced by Thirion [1], and its variants [2,3]. Recently, Gu et al. [4] implemented the original version and the variants of the demons algorithm on the GPU using the CUDA programming environment to improve the efficiency for online ART applications. However, in previous demons-based DIR methods, the voxel-based deformation vector fields (DVFs) were employed, i.e., 256^3 for each phase in a single breathing cycle of 4D (space + time) image case,

where large number of unknowns need to be estimated, so that the computational time is extremely long and cannot realize in real time for clinical applications. So that the previous demons methods were only employed in two-phase registration, instead of computing the deformations between all respiration phases, such as 10 or more. Besides that, in reality, different organs may have different motions in 4D case, such as during respiration, the lung, diaphragm and liver slide against the thoracic cage while moving independently. So it is necessary to consider the anisotropic motion fields between different organs, instead of using a global motion model.

The computational time and accuracy of current DIR approaches are still insufficient for online ART, especially in a large data sets of 4D images. The objective of this work is to propose a new DIR framework, with fast computational speed and high accuracy, by using feature-based adaptive tetrahedral meshing and GPU-based parallelization. The mesh-based geometry restricts the solution space of the image registration problem with much fewer degrees of freedom and ensures the smoothness of the transformation by interpolation. Meanwhile, the feature-based adaptive tetrahedral mesh can effectively and precisely describe the deformations according to the organ shapes and fine structures in the region of interest. In order to further improve the computational speed and make the DIR system suitable for routine clinical use, with the help of a fast local search based on the L-BFGS optimization method [5] and a single GPU-based implementation, the proposed DIR algorithm can be accomplished around 50 s for a 10-phase 4D CT with a phase dimension of $256 \times 256 \times 150$.

In the remainder of this paper, we take 4D CT images as examples, while the presented method is principally applicable to general modality images, such as MRI, ultrasound, CBCT, PET, SPECT, etc.

2 Method

2.1 Feature-Based Adaptive Tetrahedral Mesh Generation

In this section, we use a 4D NCAT phantom [6] to demonstrate the detailed procedure of the proposed finite element method (FEM), i.e., generating the high-quality and high-fidelity feature-based adaptive tetrahedral mesh.

In the feature-based mesh generation, a density field is designed to match the volume image features at first. Original images are pre-analyzed using a Laplacian operator (i.e., searching for zero crossings in the second derivative of the image to find edges) to extract features including contour edges and boundaries between organs and tissues, which are regions of highly non-linear intensity variation. When the feature edges of the volume image are obtained, a smooth density field could be calculated without manual segmentation (Fig. 1 (b)), which is designed based on the distance between the feature edges and the voxels in the volume domain. Then, the mesh vertices are automatically computed by particle-based volume meshing method, which is extended from Zhong et al.'s adaptive surface meshing framework [7]. This method is more efficient compared

with other meshing methods [8,9,10,11] as it only optimizes the vertex positions and finally computes the mesh connectivities once. Regarding each mesh vertex as a particle, the potential energy between particles determines the inter-particle forces. To generate the adaptive meshing, the concept of high-dimensional embedding space [12] is applied. In our image-based adaptive meshing scenario, such embedding space is transformed from the original Euclidean space with a density field. When the forces applied on each particle reach an equilibrium state in this embedding space, the particle distribution on the original domain will exhibit the desired adaptive property, i.e., conforming to the user-defined density field. This property is used to formulate the particle-based adaptive tetrahedral meshing framework.

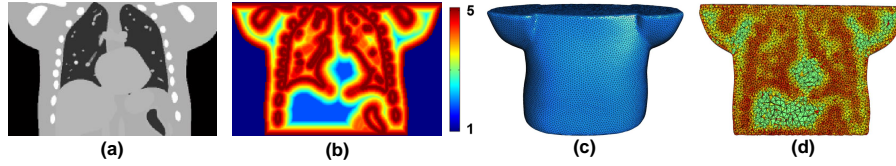


Fig. 1: Demonstration of the feature-based mesh generation on a digital 4D NCAT phantom. (a) The original image at the reference phase; (b) density field based on extracted feature edges; (c) boundary meshes well preserved the body surface; (d) a 2D view of the interior meshes with color-mapping.

The inter-particle energy \bar{E}^{ij} between particles i and j in the embedding space is defined as:

$$\bar{E}^{ij} = e^{-\frac{(\mathbf{v}_i - \mathbf{v}_j)^T \mathbf{M}_{ij} (\mathbf{v}_i - \mathbf{v}_j)}{4\sigma^2}}, \quad (1)$$

where \mathbf{v}_i and \mathbf{v}_j indicate the positions of particles i and j . \mathbf{M}_{ij} is the density field between particles i and j . It is a 3×3 diagonal matrix, and the main diagonal elements are density values. σ is Gaussian kernel width. It has been shown in [7] that the best adaptive mesh quality can be achieved when Gaussian kernel width is set as $\sigma = 0.3\sqrt{|\Omega|/N_v}$, where $|\Omega|$ is the image volume in the embedding space and N_v is the total number of particles. The gradient of \bar{E}^{ij} can be considered as the inter-particle force $\bar{\mathbf{F}}^{ij}$ in the embedding space:

$$\bar{\mathbf{F}}^{ij} = \frac{\partial \bar{E}^{ij}}{\partial \bar{\mathbf{v}}_j} = \frac{\mathbf{Q}_{ij}(\mathbf{v}_i - \mathbf{v}_j)}{2\sigma^2} e^{-\frac{(\mathbf{v}_i - \mathbf{v}_j)^T \mathbf{M}_{ij} (\mathbf{v}_i - \mathbf{v}_j)}{4\sigma^2}}, \quad (2)$$

where $\mathbf{Q}_{ij} = \sqrt{\mathbf{M}_{ij}}$ and $\bar{\mathbf{v}}_j$ is the particle j 's position in the embedding space.

The inter-particle energy defined in Eq. (1) and force defined in Eq. (2) are used to minimize the total inter-particle energy. During the optimization, the particles need to be constrained inside the torso volume; so for each iteration, the updated particles have to be projected to their nearest locations on the torso surface, if they are out of the surface. The final adaptive tetrahedral mesh can be generated by using the Delaunay triangulation method according to the optimized particle positions. In the 4D NCAT phantom and clinical data set, it

needs 40 s for the mesh generation (i.e., 10,000 vertices of feature-based adaptive tetrahedral mesh). It is noted that the mesh generation step only needs to be computed once before DIR optimization.

The regions of highly non-linear intensity variation are densely positioned by vertices, while regions of constant or linear intensity variation are assigned fewer vertices. Following this process, vertex locations are conforming to the density field as illustrated in Fig. 1 (b). As a result, meshes corresponding to boundaries between organs and tissues are denser. The color-coded tetrahedrons of the generated feature-based mesh in Fig. 1 (c), (d) illustrate that the tetrahedral volumes are well conforming to the desired density defined by the features of the given image as well as the body surface. Since most deformations occur around the boundaries between organs and tissues, edges of contours, it is desirable to place more vertices (or sampling points) at features, while fewer vertices in non-feature regions. In this way, if DVF is specified to each mesh vertex, the organ boundaries and other important features can be directly represented by the displacements of sampling points or represented by smaller-sized tetrahedrons, rather than interpolating through four vertices of one larger-sized tetrahedron. Then the deformation can be diffused from the mesh vertices to each voxel of the volume more accurately and smoothly via interpolation as follows:

$$\mathbf{D} = \text{bary}(\mathbf{W}), \quad (3)$$

where \mathbf{W} denotes the DVF specified on mesh vertices, and \mathbf{D} denotes the DVF specified on voxels. *bary* denotes the barycentric interpolation, which is similar with the trilinear interpolation. The displacement vector of each voxel is obtained through interpolating the DVF on mesh vertices by using the barycentric coordinates [13] of each voxel in its corresponding tetrahedron. Therefore, the proposed FEM restricts the solution space of the image registration problem with much fewer degrees of freedom, with considering the organ shapes and image features, and ensures the smoothness of the transformation \mathbf{W} by interpolation.

2.2 Mesh-Based DIR

In this section, we present the details of the proposed mesh-based DIR method. First, the basic framework of the DIR problem is proposed, and then the optimization strategy is provided; finally, we introduce how to accelerate the speed by using the GPU-based parallelization.

Basic Framework

Suppose there are totally T phases in a 4D image (i.e., CT, MRI, or ultrasound), $\boldsymbol{\mu} = \{\boldsymbol{\mu}^t | t = 0, \dots, T-1\}$ denotes the intensity of all phases. Once the reference phase 0 is known and a motion model is available, the other phases $[1, \dots, T-1]$ of the 4D image can be described as:

$$\boldsymbol{\mu}^t = \boldsymbol{\mu}^0(\mathbf{x} + \mathbf{d}^{0 \rightarrow t}) = \boldsymbol{\mu}^0(\mathbf{x} + \text{bary}(\mathbf{w}^{0 \rightarrow t})), \quad (4)$$

where $\mathbf{d}^{0 \rightarrow t}$ can be considered as a voxel-based motion model from phase 0 to phase t , computed according to the interpolation of the DVF $\mathbf{w}^{0 \rightarrow t}$ specified by

the mesh model in Eq. (3), and here it is the deformation matrix to transform 4D image from phase 0 to any phase $t, t \in [1, \dots, T-1]$.

The DVF $\mathbf{w}^{0 \rightarrow t}$ can be computed by minimizing the energy function E , which includes two terms: the data fidelity $E_{fid}(\mathbf{w}^{0 \rightarrow t})$ between the images of two phases and the regularization $E_{reg}(\mathbf{w}^{0 \rightarrow t})$ used to achieve smoothness constraint of the mesh-based DVF. The total energy function considering all T phases is:

$$E(\mathbf{W}) = \sum_{i=0}^{T-1} [\|\boldsymbol{\mu}^t - \boldsymbol{\mu}^0(\mathbf{x} + \text{bary}(\mathbf{w}^{0 \rightarrow t}))\|_{l_2}^2 + \beta L(\mathbf{w}^{0 \rightarrow t})], \quad (5)$$

where β is a parameter that controls the tradeoff between the data fidelity and the smoothness constraint of the DVF. $\mathbf{W} = \{\mathbf{w}^{0 \rightarrow t} | t = 0, \dots, T-1\}$. $L(\mathbf{w}^{0 \rightarrow t})$ is the smoothness constraint term defined as:

$$L(\mathbf{w}^{0 \rightarrow t}) = \sum_{i=1}^{N_i} \sum_{d=1}^3 \left[\left(\frac{\sum_{k \in N_i} (\mathbf{w}_k^{0 \rightarrow t}(d) - \mathbf{w}_i^{0 \rightarrow t}(d))}{|N_i|} \right)^2 \right], \quad (6)$$

where is a summation of the square of Graph Laplacian operations on the DVF (including three components: $d = 1, 2, 3$) over every vertex. N_v is the total number of the mesh vertices. N_i is the set of one-ring neighboring vertices (k) of vertex i . $|N_i|$ is the size of set N_i .

Optimization

(1) Gradient of DIR Energy The gradient of $E(\mathbf{W})$ w.r.t. $\mathbf{w}_i^{0 \rightarrow t}$ at mesh vertex i can be considered as:

$$\begin{aligned} \frac{\partial E(\mathbf{W})}{\partial \mathbf{w}_i^{0 \rightarrow t}} &= -2[\boldsymbol{\mu}^t - \boldsymbol{\mu}^0(\mathbf{x} + \text{bary}(\mathbf{w}^{0 \rightarrow t}))] \frac{\partial \boldsymbol{\mu}^0(\mathbf{x} + \text{bary}(\mathbf{w}_i^{0 \rightarrow t}))}{\partial \mathbf{w}_i^{0 \rightarrow t}} \\ &- 2 \sum_{d=1}^3 \left[\left(\frac{\sum_{k \in N_i} (\mathbf{w}_k^{0 \rightarrow t}(d) - \mathbf{w}_i^{0 \rightarrow t}(d))}{|N_i|^2} \right) \right] + 2 \sum_{d=1}^3 \left[\left(\frac{\sum_{k \in N_i} (\mathbf{w}_i^{0 \rightarrow t}(d) - \mathbf{w}_k^{0 \rightarrow t}(d))}{|N_k|^2} \right) \right]. \end{aligned} \quad (7)$$

It is noted that the regularization terms are symmetrically defined on every mesh vertex and its neighbors, so there are two terms in the gradient of DVF at mesh vertex i . Since the energy function Eq. (5) is a quadratic form of \mathbf{W} and its gradients as shown in Eq. (7), it is clear to see that the total energy $E(\mathbf{W})$ is C^2 . This is a significant good property during the optimization: the C^2 continuity can ensure to obtain a good optimal result, instead of trapping into some local minima.

(2) L-BFGS Method Due to the smoothness (C^2 continuity) of the energy function with the explicit gradient formula, it is therefore possible to minimize the mesh-based DIR energy function using Newton-like optimization methods and expect fast convergence. Specifically, we use the L-BFGS algorithm [5], a quasi-Newton method, to optimize the DVF, which can quickly find the minimum of the energy for our DVF estimation. It converges in fewer optimization steps than the demons DIR methods [1,2,3] with iterative gradient for DVF

computation. For each iteration of L-BFGS optimization, we update the energy $E(\mathbf{W})$ by summing the fidelity and regularization terms over all phases, and update its gradients $\frac{\partial E}{\partial \mathbf{w}_i^{0 \rightarrow i}}$ on each mesh vertex. The L-BFGS method computes the approximated inverse Hessian matrix by accumulating the gradients over a small fixed number of preceding iterations. Both the memory complexity and the computational cost of each iteration of L-BFGS are $O(n)$, where n is the number of variables, here it is the number of mesh vertices. The energy optimization by L-BFGS method can converge very quickly in 100 iterations for all our experimental images.

GPU-Based Parallel Acceleration

The entire process of this 4D image DIR method is implemented on GPU. The GPU card used in our experiments is an NVIDIA GeForce GTX Titan Z with 12GB GDDR5 video memory. It has 5760 CUDA cores. Utilizing such a GPU card with tremendous parallel computing ability can significantly increase the computational efficiency. There are four GPU-based computational sections (i.e., regularization computation, deformed volume image computation, data fidelity computation, and gradient of total energy) during the DIR. It is straightforward to accomplish all the computations in parallelism, since these four sections can be either parallel based on each mesh vertex or each voxel.

3 Results

3.1 4D NCAT Digital Phantom

In this study, ten breathing phases of the 4D NCAT phantom were generated. The maximum diaphragm motion was 20 *mm* and the maximum chest anterior-posterior motion was 12 *mm* during the respiration. A spherical 3D tumor with diameter of 10 *mm* was also simulated as shown in Row 1 of Fig. 2. The dimensions of the phantom were $256 \times 256 \times 150$ with voxel size of $2 \times 2 \times 2$ *mm*³.

The adaptive tetrahedral mesh on the torso was created with about 10,000 vertices from the reference phase 0 of 4D CT as shown in Fig. 1. Fig. 2 shows deformed images and motions of the 4D NCAT phantom at phase 0 (end-expiration), phase 2, phase 4 (end-inspiration), phase 6, and phase 8 from coronal views by using the proposed mesh-based DIR method. The image details are well preserved for bony, lung, tumor, and other fine structures, and meanwhile, the motions of the lung and tumor are well captured. So that both the image and motion visualization are accurately computed. The red dot lines go through the diaphragm and tumor center of coronal view images and surfaces at phase 0, respectively, to further illustrate the performance of the proposed DIR method. From DVF visualization (both the directions and magnitudes are computed and compared based on phase 0), the feature-based adaptive mesh can be well captured the complicated anisotropic motions as shown in the zoom-in part of Fig. 2 that the tissues and tumor inside the lung are moving downward, while the thoracic cage is moving upward from end-expiration to end-inspiration.

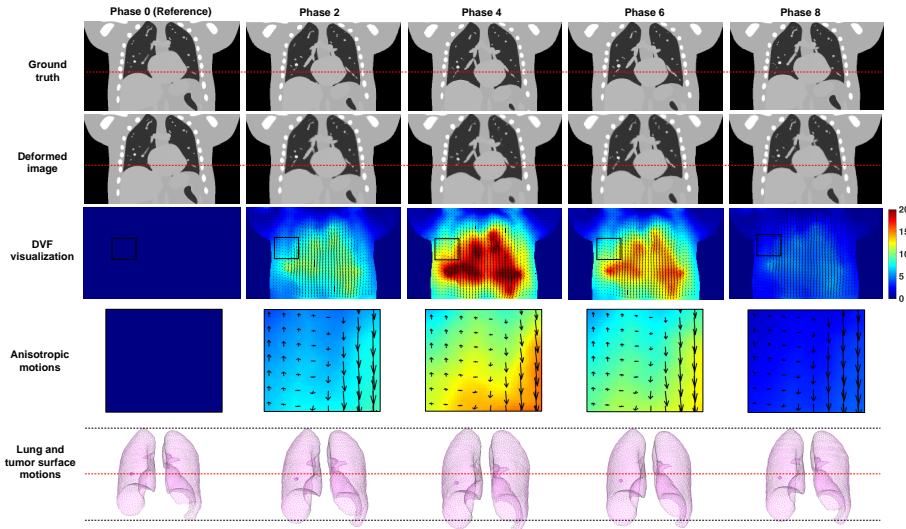


Fig. 2: The deformed images and motions of the 4D NCAT phantom at phase 0 (end-expiration), phase 2, phase 4 (end-inspiration), phase 6, and phase 8 from coronal views.

Table 1: Evaluations of deformed image accuracy and motion accuracy (*mm*) of tumor center and lung surface on different phases.

Phase	2	4	6	8
NCC	0.9965	0.9859	0.9945	0.9992
NRMSE	0.0708	0.1426	0.0893	0.0345
Tumor center	0.6850	1.1450	0.7750	0.5600
Lung surface	1.5028	2.6061	2.0476	1.3513

Tab. 1 reports the quantitative evaluations on all deformed images by using conventional normalized cross correlation (NCC) and normalized root mean square error (NRMSE) measurements. It also reports the evaluations on motions of the tumor center and lung surfaces. As for the tumor center, it is measured by using the 3D distance error between the center of the tumor computed based on the DVFs and tumor center generated by manual segmentation. As for the motions of the lung surfaces, we use Hausdorff distance to measure the approximation accuracy of the deformed surfaces based on DVFs to the isosurface generated by manual segmentation. All of the quantitative results show that the proposed DIR method has very small errors (at most around one voxel size at largest deformed phase), so that it can be used as an automated and effective segmentation method to transfer tumor or organ contours/surfaces from the reference planning image to other daily images, without tedious manual segmentation. The overall computational time of a 4D $256 \times 256 \times 150$ image with 10 phases is 51.60 s ($< 1\text{ m}$). However, the computational time of the voxel-based DIR method on CPU is much slower, i.e., about 9652 s ($> 160\text{ m}$), such as demons (without multi-scale strategy) [1,2,3]. Therefore, the proposed method has dramatically improved the running speed and makes it possible to reach our

ultimate target to develop a less-than-1-minute 4D DIR-based visualization and motion tracking system for its clinical applications.

3.2 Clinical Data Set

Finally, a clinical evaluation study was performed on thoracic 4D CT images obtained from a clinical case [14]. The patients were treated for esophageal cancer and the 4D CT images of the thorax and upper abdomen were obtained. Fig. 3 shows deformed images and motions of the 4D clinical CT at phase T00 (end-inspiration) and phase T50 (end-expiration) from coronal views by using the proposed mesh-based DIR method. The inhaling lung surface is generated by computing the isosurface from the segmented lung masks manually. The exhaling lung surface is deformed based on the inhaling lung surface with the DVF obtained in the proposed DIR method. As for the quantitative evaluations, NCC and NRMSE between the deformed image and the ground truth (target) image at phase T50 are 0.9950 and 0.0815.

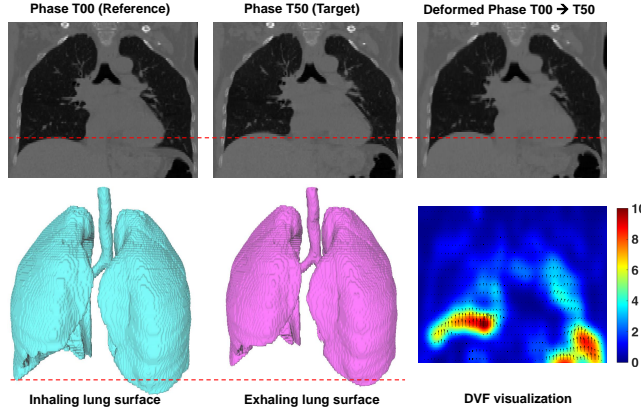


Fig. 3: The deformed images and motions of the 4D clinical CT at phase T00 (end-inspiration) and phase T50 (end-expiration) from coronal views.

Besides that, accuracy evaluation of our proposed method is also based on landmark features identified in the reference and target images by thoracic imaging experts on 4DCT1 with dimensions of $256 \times 256 \times 94$ and voxel size of $0.97 \times 0.97 \times 2.5 \text{ mm}^3$, which are publicly available on www.dir-lab.com. The number of feature point pairs on this case is 1280, and the average landmark displacement is 4.01 mm . Registration error was determined by applying the DVFs to the landmark coordinates on the reference image, then comparing the result to the corresponding landmark coordinates on the target image. The mean (and standard deviation) of 3D distance error (mm) for the proposed DIR is 1.0641 (1.0578), which are smaller than the demons methods as reported in [4].

4 Conclusion

In this work, we have developed a feature-based adaptive mesh technique for 4D DIR with considering complicated motions of different organs and image

features, and a GPU-based parallel algorithm to further improve the efficiency to reach an aim of being real-time (51.60 s for $256 \times 256 \times 150 \times 10$ phases of DVFs and images). Once the system is built, it is feasible and effective to be used in collaborative visualization, tumor-identification and segmentation, registration and tracking of deformable organs, in real time. We use the 4D CT (a phantom and a clinical data set) as examples to demonstrate our algorithm; definitely, this framework can be extended to non-linearly register medical imaging data with different modalities, such as 4D-MRI, 4D-Ultrasound, 4D-PET, 4D-SPECT, etc. Extensive comparisons between our method and existing approaches in clinical practice will be conducted in the near future.

References

1. Thirion, J. P.: Image matching as a diffusion process: an analogy with Maxwell's demons. *Med. Image Anal.* 2, 243–246 (1998)
2. Wang, H., Dong, L., O'Daniel, J., Mohan, R., Garden, A., Ang, K., Kuban, D., Bonnen, M., Chang, J., Cheung, R.: Validation of an accelerated 'demons' algorithm for deformable image registration in radiation therapy. *Phys. Med. Biol.* 50, 2887–2905 (2005)
3. Yang, D., Li, H., Low, D., Deasy, J., El Naqa, I.: A fast inverse consistent deformable image registration method based on symmetric optical flow computation. *Phys. Med. Biol.* 53, 6143–6165 (2008)
4. Gu, X., Pan, H., Liang, Y., Castillo, R., Yang, D., Choi, D., Castillo, E., Majumdar, A., Guerrero, T., Jiang, S.: Implementation and evaluation of various demons deformable image registration algorithms on GPU. *Phys. Med. Biol.* 55, 207–219 (2010)
5. Liu, D. C., Nocedal, J.: On the limited memory BFGS method for large scale optimization. *Mathematical Programming.* 45, 503–528 (1989)
6. Segars, W. P.: Development and application of the new dynamic NURBS-based Cardiac-Torso (NCAT) phantom. Ph.D. dissertation, University of North Carolina. (2001)
7. Zhong, Z. C., Guo, X. H., Wang, W. P., Lévy, B., Sun, F., Liu, Y., Mao, W. H.: Particle-based anisotropic surface meshing. *ACM Trans. Graph.* 32, 99:1–99:14 (2013)
8. Shimada, K., Yamada, A., Itoh, T.: Anisotropic triangular meshing of parametric surfaces via close packing of ellipsoidal bubbles. 6th International Meshing Roundtable. 375–390 (1997)
9. Du, Q., Wang, D.: Anisotropic centroidal Voronoi tessellations and their applications. *SIAM Journal on Scientific Computing.* 26, 737–761 (2005)
10. Valette, S., Chassery, J. M., Prost, R.: Generic remeshing of 3D triangular meshes with metric-dependent discrete Voronoi diagrams. *IEEE Transactions on Visualization and Computer Graphics.* 14, 369–381 (2008)
11. Boissonnat, J., Wormser, C., Yvinec, M.: Anisotropic Delaunay mesh generation. *SIAM J. Comput.* 44, 467–512 (2015)
12. Nash, J.: C^1 -isometric embeddings. *Annals of Mathematics.* 60, 383–396 (1954)
13. Coxeter, H.: Introduction to geometry (2nd ed.). John Wiley and Sons. 216–221 (1969)
14. Castillo, R., Castillo, E., Guerra, R., Johnson, V.E., McPhail, T., Garg, A.K., Guerrero, T.: A framework for evaluation of deformable image registration spatial accuracy using large landmark point sets. *Phys Med Biol.* 54, 1849–1870 (2009)